Simulation of ultrasonic pulse propagation through the abdominal wall

T. Douglas Mast,[a] Laura M. Hinkelman,[b] and Michael J. Orr
Department of Electrical Engineering, University of Rochester, Rochester, New York 14627

Victor W. Sparrow
Graduate Program in Acoustics, The Pennsylvania State University, University Park, Pennsylvania 16802

Robert C. Waag
Departments of Electrical Engineering and Radiology, University of Rochester, Rochester, New York 14627

(Received 1 August 1996; accepted for publication 19 March 1997)

Ultrasonic pulse propagation through the human abdominal wall has been simulated using a model for two-dimensional propagation through anatomically realistic tissue cross sections. The time-domain equations for wave propagation in a medium of variable sound speed and density were discretized to obtain a set of coupled finite-difference equations. These difference equations were solved numerically using a two-step MacCormack scheme that is fourth-order accurate in space and second-order accurate in time. The inhomogeneous tissue of the abdominal wall was represented by two-dimensional matrices of sound speed and density values. These values were determined by processing scanned images of abdominal wall cross sections stained to identify connective tissue, muscle, and fat, each of which was assumed to have a constant sound speed and density. The computational configuration was chosen to simulate that of wavefront distortion measurements performed on the same specimens. Qualitative agreement was found between those measurements and the results of the present computations, indicating that the computational model correctly depicts the salient characteristics of ultrasonic wavefront distortion *in vivo*. However, quantitative agreement was limited by the two-dimensionality of the computation and the absence of detailed tissue microstructure. Calculations performed using an asymptotic straight-ray approximation showed good agreement with time-shift aberrations predicted by the full-wave method, but did not explain the amplitude fluctuations and waveform distortion found in the experiments and the full-wave calculations. Visualization of computed wave propagation within tissue cross sections suggests that amplitude fluctuations and waveform distortion observed in ultrasonic propagation through the abdominal wall are associated with scattering from internal inhomogeneities such as septa within the subcutaneous fat. These observations, as well as statistical analysis of computed and observed amplitude fluctuations, suggest that weak fluctuation models do not fully describe ultrasonic wavefront distortion caused by the abdominal wall. [S0001-4966(97)00308-1]

PACS numbers: 43.80.Cs, 43.20.Fn, 43.58.Ta [FD]

INTRODUCTION

Much has recently been written on the distortion of ultrasonic wavefronts by tissue inhomogeneities and its effect on ultrasonic images. Direct measurements of the ultrasonic distortion produced by human abdominal wall,[1,2] chest wall,[3] and breast[4–6] have been made and techniques for the correction of this distortion have been proposed and examined.[7–15] However, the physical causes of ultrasonic wavefront distortion by human soft tissues are not yet well understood.

Several investigators have set out to improve this understanding by devising models of human tissue to explain observed distortions. Robinson *et al.*[16] and Sauerbrei[17] were able to explain shadowing, enhancement, and double image artifacts seen in abdominal imaging via ray tracing through arrangements of homogeneous structures, each with a different characteristic sound speed and a simple geometric shape. More recently, Manry and Broschat[18] applied a finite-difference time-domain (FDTD) algorithm to a similarly simple model to study ultrasonic propagation through the breast. A Dutch group[19] has developed a method to calculate acoustic transmission and reflection at an irregularly shaped boundary between layers of two homogeneous media. However, none of these models takes into account the detailed structure of human tissues or the complex arrangement of these tissues in the human body. One early study used power spectra of sectional images to determine scattered power of porcine liver tissue under the Born approximation.[20] A recent study of the effect of tissue microstructure on ultrasonic imaging has been performed by a group at the Riverside Research Institute[21] using sound-speed maps determined from acoustic microscopy images of liver cross sections. Simulations of a-scan and b-scan mode imaging were performed by convolving idealized pulses with estimated tissue impulse-

[a]Current affiliation: Applied Research Laboratory, The Pennsylvania State University, University Park, PA 16802.
[b]Current affiliation: Department of Meteorology, The Pennsylvania State University, University Park, PA 16802.

response functions. While this approach provides insight into the relationship between tissue microstructure and speckle, the linear convolution process does not model distortion effects such as beam and focus degradation.

Models of ultrasonic propagation through distorting layers, whether stated explicitly or implicitly, are essential to all distortion correction methods. Many use models of the types described above. For example, Kossoff *et al.*[7] have been able to reduce gross artifacts caused by refractive effects in the abdomen. Smith *et al.*[8] found that distortions created by imaging through the skull could be corrected by compensating for refraction by a plane layer, but had little success when viewing the abdominal wall as a plane layer of fat. Others followed the lead of those working on distortion encountered in astronomy and modelled the distorting tissue as a phase screen at the receiving aperture,[9–11] which implies that received waveforms differ only in phase. One notable exception is an early paper by Hirama *et al.*,[12] who used a phase and amplitude screen at or away from the aperture. Substantial recent experimental evidence has confirmed that the distortion produced by actual tissues is more complicated than that produced by a single phase screen at the receiving aperture.[2,3,5,6,22] For this reason, some investigators[13,14] have employed a phase screen placed some distance from the aperture, so that amplitude and wave shape variations as well as arrival time differences can be accounted for. Others[15] have approximated this configuration using both a phase and an amplitude screen at the aperture.

Models of wavefront distortion are also important because they are used to test distortion correction algorithms. Very few of these techniques have been tested using ultrasonic signals recorded after propagation through actual human tissues.[7,8,13] Instead, most investigators have relied on computer simulations in which phase and/or amplitude distortion is numerically added to received or calculated waveforms.[9–12,15] Others have used data from experiments in which an aberrator constructed of a uniform medium with varying thickness is inserted between the ultrasonic transducer and the target.[9,10,12,14]

While some of the proposed algorithms perform well under these simplified conditions, none has been able to return an ultrasonic beam or image distorted by human tissues to diffraction-limited quality. Such focus correction is theoretically possible; for instance, a wavefront emitted by a point source and distorted by propagation through an inhomogeneous medium is optimally refocused by propagating the time-reversed wavefront back through the same inhomogeneity.[14] The limitations of current methods may, in part, be due to the fact that each method rests on unrealistic assumptions about the nature of distortions produced clinically. For example, human tissues are not completely homogeneous, organs rarely occur in simple geometric shapes, and the thickness of the abdominal wall, chest wall, or intervening tissue of the breast is generally a significant fraction of the transducer focal length. A better understanding of the composition and structure of the body wall, breast, or other distorting tissues and their interaction with ultrasound would clearly aid the development of aberration correction techniques.

The purpose of the present study is to simulate ultrasonic propagation through the abdominal wall using a realistic model of tissue structure and a computational model that incorporates all wave effects such as single and multiple scattering, reflection, and refraction. The model is shown to produce distortion similar to experimental measurements. Results were also obtained using an asymptotic straight-ray approximation. Examination of the detailed wave propagation computed with the finite-difference model provides previously unavailable insight into the physical nature of ultrasonic wavefront distortion. The results suggest that simple phase screen models can explain some of the time-shift aberrations caused by the human abdominal wall, but that consideration of strong scattering effects is necessary to explain experimentally measured amplitude and waveform distortion.

I. THEORY

Ultrasonic pulse propagation through the human abdominal wall was modelled using the equations of motion for a lossless fluid with variable sound speed and density. The tissue was assumed to be motionless except for small acoustic perturbations. For such a fluid, the linearized equations of mass conservation, momentum conservation, and state are respectively

$$\frac{\partial \rho'(\mathbf{r},t)}{\partial t} + \nabla \cdot (\rho(\mathbf{r})\mathbf{v}(\mathbf{r},t)) = 0, \tag{1}$$

$$\rho(\mathbf{r}) \frac{\partial \mathbf{v}(\mathbf{r},t)}{\partial t} = -\nabla p(\mathbf{r},t), \tag{2}$$

$$\frac{\partial p(\mathbf{r},t)}{\partial t} = c(\mathbf{r})^2 \left(\frac{\partial \rho'(\mathbf{r},t)}{\partial t} + \mathbf{v}(\mathbf{r},t) \cdot \nabla \rho(\mathbf{r}) \right), \tag{3}$$

where $\rho(\mathbf{r})$ and $c(\mathbf{r})$ are the spatially dependent ambient density and sound speed, $\rho'(\mathbf{r},t)$ is the acoustic perturbation in density, $p(\mathbf{r},t)$ is the acoustic pressure, and $\mathbf{v}(\mathbf{r},t)$ is the (vector) acoustic particle velocity. The linear propagation equations (1)–(3) are obtained from the full fluid-mechanical equations by removing all terms of quadratic or higher order in the acoustic perturbation variables ρ', p, and $\mathbf{v}$.[23]

Equation (3) may be used to eliminate the acoustic density perturbation from Eqs. (1) and (2). This yields, in two-dimensional Cartesian coordinates, the coupled equations

$$\frac{\partial p(x,y,t)}{\partial t} + \rho(x,y) c(x,y)^2 \nabla \cdot \mathbf{v}(x,y,t) = 0, \tag{4}$$

$$\rho(x,y) \frac{\partial \mathbf{v}(x,y,t)}{\partial t} + \nabla p(x,y,t) = 0. \tag{5}$$

Equations (4) and (5) were solved numerically using a finite-difference time-domain (FDTD) method. In order to implement the finite-difference algorithm, the fluid-mechanical equations were written in the form

$$\frac{\partial \mathbf{S}(x,y,t)}{\partial t} + \frac{\partial \mathbf{F}(\mathbf{S}(x,y,t))}{\partial x} + \frac{\partial \mathbf{G}(\mathbf{S}(x,y,t))}{\partial y} = 0, \tag{6}$$

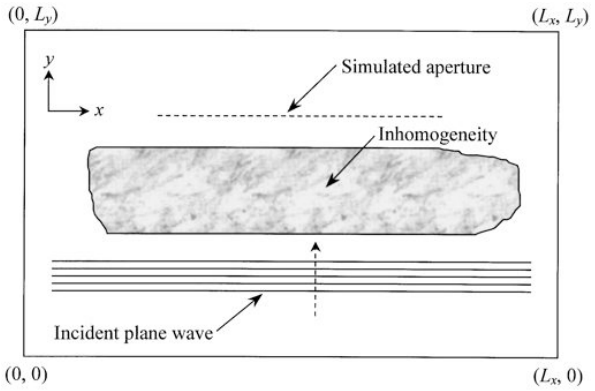

FIG. 1. Computational domain for finite-difference time-domain calculations. A plane wave pulse propagates in the y direction through water, shown as the white background, and an inhomogeneous region, shown here as a textured object. The acoustic pressure is recorded by a number of simulated transducer elements beyond the inhomogeneity.

where the ordered triplets $\mathbf{S}(x,y,t)$, $\mathbf{F}$, and $\mathbf{G}$ are defined

$$\mathbf{S}=\left(\frac{p}{\rho c^2},\rho u,\rho v\right),\quad \mathbf{F}=(u,p,0),\quad \mathbf{G}=(v,0,p), \tag{7}$$

and u and v, respectively, are the $\mathbf{x}$ and $\mathbf{y}$ components of the acoustic velocity.

The system of equations expressed in Eq. (6) was numerically solved using a two-step MacCormack algorithm that was fourth-order accurate in space and second-order accurate in time.[24,25] The implementation of the finite-difference operators was equivalent to that described in Ref. 26. The initial condition was chosen to simply model the experimental condition of a slowly-varying, nearly planar wavefront emitted from a wide band, pulsed, point-like source far from the tissue layer. The initial wavefront was represented as a plane wave pulse propagating in the $+y$ direction,

$$\begin{aligned} &p(x,y,0)=-\sin(k_0(y-y_0))e^{-(y-y_0)^2/(2\sigma^2)},\\ &u(x,y,0)=0,\quad v(x,y,0)=\frac{p(x,y,0)}{\rho c}, \end{aligned} \tag{8}$$

where the wave number k_0 is equal to $2\pi f_0/c$ for a center frequency of f_0 and σ is the Gaussian parameter of the pulse temporal envelope. The Gaussian parameter σ was chosen to simulate the bandwidth of the pulse used in the experiments, as discussed below in Sec. II.

The computational configuration is sketched in Fig. 1. The domain of computation is two-dimensional, with the y direction taken to be parallel to the direction of propagation and the x direction parallel to the initial wavefront. Periodic boundary conditions were applied on the edges of the grid parallel to the direction of propagation, that is,

$$\mathbf{S}(0,y,t)=\mathbf{S}(L_x,y,t). \tag{9}$$

The periodic boundary conditions, together with the plane wave initial condition, ensured that the wavefront remained undistorted in the absence of propagation-path inhomogeneities. On the edges normal to the direction of propagation, radiation boundary conditions were applied to calculate p and v. These conditions were chosen to absorb waves normally incident to the boundaries $y=0$ and $y=L_y$, so that waves propagating in directions close to normal would incur only small reflections. The radiation conditions, equivalent to unidirectional wave equations applied at the top and bottom boundaries, were

$$\begin{aligned} &\frac{\partial p}{\partial t}=c\frac{\partial p}{\partial y},\quad \frac{\partial v}{\partial t}=c\frac{\partial v}{\partial y},\quad \text{for } y=L_{yi},\\ &\frac{\partial p}{\partial t}=-c\frac{\partial p}{\partial y},\quad \frac{\partial v}{\partial t}=-c\frac{\partial v}{\partial y},\quad \text{for } y=0. \end{aligned} \tag{10}$$

The derivatives in Eqs. (10) were calculated using first-order-accurate differences, and the estimated time derivatives of p and v were used to advance the solution on the top and bottom boundaries after differencing was performed on the interior of the grid.

II. METHOD

The accuracy of the finite-difference method in this study was tested using a benchmark scattering computation. The benchmark problem, which was chosen to approximate the realistic problem of scattering from a single fat lobule while allowing the possibility for comparison with a known exact solution, was the scattering of a single-frequency, 3.75-MHz plane wave by a cylinder of diameter 4.0 mm with sound speed and density values equal to 95% of background. These parameters correspond approximately to the contrast and size of a typical fat lobule in a water background. The finite-difference computation was implemented using the methods detailed above, with a plane-wave radiation condition [Eqs. (10)] on the top boundary and periodic boundary conditions on the side boundaries. The incident wave was generated by the oscillating-wall boundary condition

$$v(x,0,t)=\sin(2\pi f_0 t), \tag{11}$$

where f_0 was 3.75 MHz.

The total pressure field obtained using the finite-difference method was compared with the total pressure calculated from an exact solution for scattering from the same cylinder.[27] The pressure was compared using a simulated aperture of 154 point receivers extending 12 mm in the x direction and located 1 mm above the cylinder boundary in the y direction. As seen in Fig. 2, the amplitude and phase of the pressure calculated with the finite-difference method agree very well with those predicted by the exact solution. This agreement is quantified by the L^2 error[28] between the total pressure from the finite-difference solution and the exact solution, defined as

$$\epsilon=\sqrt{\left(\sum |\hat{p}_{\text{fd}}-\hat{p}_{\text{exact}}|^2\right)\Big/\left(\sum |\hat{p}_{\text{exact}}|^2\right)}, \tag{12}$$

where $\hat{p}_{\text{fd}}$ and $\hat{p}_{\text{exact}}$ are Fourier components of the pressure calculated from the finite-difference algorithm and the exact solution, respectively. The agreement achieved corresponds to an L^2 error $\epsilon=0.015$.

Five fresh unfixed abdominal wall sections, each from a different donor, were obtained from autopsy and stored at $-20\,^{\circ}\text{C}$. Each specimen was later thawed by immersion in room-temperature saline solution, and a grid with 1-cm spac-

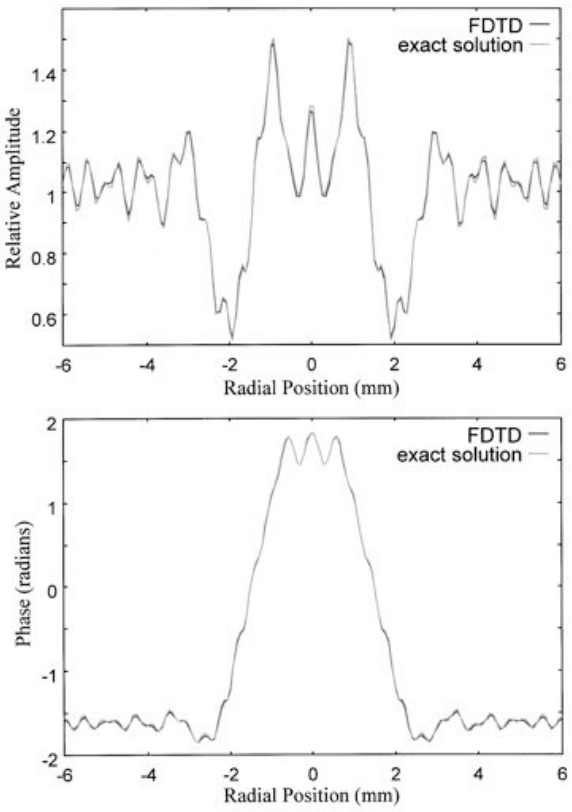

FIG. 2. Computed amplitude and phase for transmission through a fat-mimicking cylinder. Results are shown for an exact solution and for the finite-difference, time-domain (FDTD) solution. Top: theoretical and computed amplitude. Bottom: theoretical and computed phase.

ing oriented parallel to the array and elevation directions was ruled on its skin surface with India ink. The wavefront distortion produced by each specimen was then measured according to the procedure detailed in Ref. 2. A specimen was suspended between 7.5-μm-thick polyimide membranes in a water tank electronically maintained at 37.0 °C. Ultrasonic pulses at a nominal center frequency of 3.75 MHz were emitted from a custom-made, 13-mm-diam, hemispheric source[29] and, after travelling a distance of approximately 165 mm, entered the specimen through its peritoneal membrane. Data were recorded on each of the 128 elements of a 3.75-MHz linear array[30] placed 5–10 mm above the specimen's skin surface. A foam mask was used to reduce the elevation dimension of the receiving array, so that the active area of each element measured 0.72×1.44 mm^2. The array was physically translated 32 times in the elevation direction to obtain data for a 92.16×46.08 mm^2 aperture. The position of each measurement relative to the grid on the specimen's skin was noted for future correlation with the tissue cross sections used in the simulations, and the specimen was then refrozen at -20 °C.

After the wavefront distortion measurements, a bandsaw was used to slice the frozen specimens lengthwise, i.e., in the measurement array direction, along the grid rulings to obtain cross sections at 1-cm intervals. Distortion or tearing of the tissue specimens was prevented by lowering the temperature of the specimens to about -80 °C by immersion in an ethanol–dry ice bath before cutting. The specimen slices were then fixed in a 10% buffered formalin solution. The cross sections were stained with a modified Gomori's trichrome stain according to the procedure detailed in Ref. 31 so that the fat, muscle, and connective tissue could be distinguished. This stain colored the muscle red and the connective tissue blue while leaving the fat its natural color. Full color 300 d.p.i. images of the cross sections were created by placing each stained tissue cross section directly onto the surface of a digital flatbed scanner. A commercial image editing package[32] was used to remove scanning artifacts such as shadows surrounding the specimens and to correct staining irregularities before the fat, muscle, connective tissue, and background were converted to uniform shades of green, red, blue, and white, respectively, by a FORTRAN program. The finished images were cropped to a length of about 110 mm to leave some margin beyond the size of the receiving aperture while minimizing the computational grid size. An additional guard band of about 10 mm of water was also added to each end of the images to prevent spurious waves (caused by wrap-around associated with the periodic boundary conditions on the sides of the domain) from affecting the signals recorded at the simulated aperture.

The density and sound speed arrays needed for the finite-difference computation were created by mapping the colors of the tissue images to reference density and sound speed values for the three tissue types and water. The water sound speed and density employed were those of pure water at body temperature (37.0 °C).[34,35] Sound speeds for muscle and fat were obtained by averaging values for human tissues given in Refs. 37 and 38. A representative sound speed for connective tissue was determined using an empirical formula relating collagen content to ultrasonic sound speed[39] together with a measured value for collagen content of human skin.[40] Density values for the tissues were determined from Ref. 41 by averaging values reported for adipose tissue, skeletal muscle, and skin, respectively. Attenuation values employed in the straight-ray computations were determined from measurements summarized in Ref. 37 for human fat at 37 °C, human biscep muscle at 37 °C, and human skin at 40 °C. Attenuation values reported at other ultrasonic frequencies were interpolated to the center frequency of 3.75 MHz assuming a linear dependence of attenuation on frequency. The attenuation for water was estimated by extrapolating frequency- and temperature-dependent attenuation summarized in Ref. 36 to 3.75 MHz and 37.0 °C. The parameter values employed in the present study are summarized in Table I.

The finite-difference program was used to simulate propagation of a plane wave pulse through each scanned cross section from the peritoneal membrane to the skin surface as in the distortion measurements. The spatial step size of the finite difference grid was chosen to be 0.0271 mm, or 1/15 wavelength in water at the center frequency of 3.75 MHz. The temporal step size was chosen for an optimal Courant–Friedrichs–Levy number $c\Delta t/\Delta x$ of 0.25.[33] The Gaussian parameter σ of the source pulse was chosen to be 0.3574 in accordance with the experimentally measured pulse bandwidth of 1.6 MHz. Visual comparison confirmed

TABLE I. Reference values for sound speed, density, and attenuation. Sound speed and density values were used in the finite-difference time-domain computation, while sound speed and attenuation values were used in the straight-ray computation.

Medium	Sound speed (mm/μs)	Density (g/cm^3)	Attenuation (dB/cm)
Water	1.524[a]	0.993[b]	0.02[c]
Fat	1.478[d,e]	0.950[g]	1.8[d]
Muscle	1.547[d]	1.050[g]	4.1[d]
Skin/CT	1.613[f]	1.120[g]	5.9[d]

[a]Reference 34.
[b]Reference 35.
[c]Reference 36.
[d]Reference 37.
[e]Reference 38.
[f]References 39 and 40.
[g]Reference 41.

that the simulated pulse closely matched the experimental pulses in shape and length.

Each simulation was performed on an individual IBM SP2 node with 1 GB of random-access memory. Finite-difference grids on the order of 5000×2000 points were employed. At each time step, the wave field was updated on a grid subset chosen to include the entire support of the acoustic wave but to exclude quiescent regions. The entire pressure field was saved as a raster image at intervals of 0.444 μs, for later visualization. Computational time for each calculation was on the order of 15 hours.

Signals were recorded for 7.3 μs at a sampling frequency of 225 MHz by 128 simulated receivers of width 0.72 mm, placed about 8 mm from the skin surface of the specimen. The simulation of receiving elements was performed by integrating the locally computed pressure over a finite width. Element directivity was included by the implicit integration of omnidirectional sensitivity functions over the width of each element.

A one-dimensional version of the reference waveform method[13] was used to calculate the arrival time of the pulse at each receiving position in the simulation data. The arrival time fluctuations across the receiving aperture caused by each cross section were calculated by subtracting a linear fit from these calculated arrival times. Energy level fluctuations in the data were calculated by summing the squared amplitudes of each waveform over a 2.4 μs window which isolated the main pulse, converting to decibel units, and subtracting the best linear fit from the resulting values. The purpose of the linear fit removal in each case was to compensate for gross changes in tissue thickness across the array. Variations in pulse shape across the aperture were evaluated using the waveform similarity factor defined in Ref. 13.

The measured data were first corrected for gross variations in arrival time caused by the measurement geometry by subtracting a fitted two-dimensional fourth-order polynomial from the measured arrival times. Waveforms measured for the elevations which corresponded most closely to the positions from which the cross sections were taken were then analyzed using the one-dimensional technique described above. The simulation and measurement results were compared to determine the accuracy of the computational model.

Arrival time and energy level fluctuations were also computed for the modelled cross sections using simpler techniques. In each case, ultrasonic rays were assumed to pass straight through the specimen without deviation from their direction of incidence. The arrival time T of each ray was calculated using the formula

$$T(x)=\int \frac{1}{c(x,y)}dy, \tag{13}$$

where the integral is performed numerically along the ray path through the tissue and water. Likewise, the energy level of each ray was computed by integrating the spatially dependent attenuation coefficient along the ray paths, so that the transmission loss in dB was given by

$$\mathrm{TL}(x)=\int \alpha(x,y)dy, \tag{14}$$

where α is the local attenuation coefficient at the center frequency of 3.75 MHz specified in dB per unit length. The sound-speed and attenuation values employed were those reported in Table I. The resulting arrival time and energy level variations were compared to the values obtained for the same cross sections using the FDTD simulation and from the experimental measurements described above.

III. RESULTS

Tissue maps for the six abdominal wall cross sections studied are presented in Fig. 3. The average thickness of the cross sections is 26.8 mm. In each case, connective tissue layers are visible at each tissue interface, the lobular structure of the fat layer is clearly shown, and the detailed intermingling of fat and connective tissue in the muscle layer is evident. The muscles that occur in these cross sections are the rectus abdominus, transversus abdominus, and external and internal obliques. Aponeuroses, or the ends of muscle sections, are evident in each image.

Example wave fields calculated using the finite-difference model are shown in Figs. 4 and 5. These two figures show acoustic pressure fields within the tissue cross section depicted in Fig. 3(f). Examination of the wavefront evolution shows the mechanism for formation of specific features that appear in the received wavefronts shown in Fig. 6.

Figure 4 shows simulated internal wavefronts within cross section 120fe during the initial propagation through muscle and connective tissue. The distinctive feature of this portion of the propagation is a large-scale time-shift fluctuation caused by propagation through a fatty aponeurosis. Since the fat contained within the aponeurosis has a lower sound speed than the surrounding muscle and connective tissue, propagation through this region causes a substantial delay in this portion of the wavefront. This delay is accumulated as the wave propagates through the aponeurosis, so that a portion of the wavefront is delayed by about 0.2 μs (about three fourths of the wave period) as shown in Fig. 4(d). The accumulated delay is also visible in the wavefront after propagation through the entire specimen, as shown in Figs. 6(f) and 7(f). Thus, the time-shift aberration occurring in this

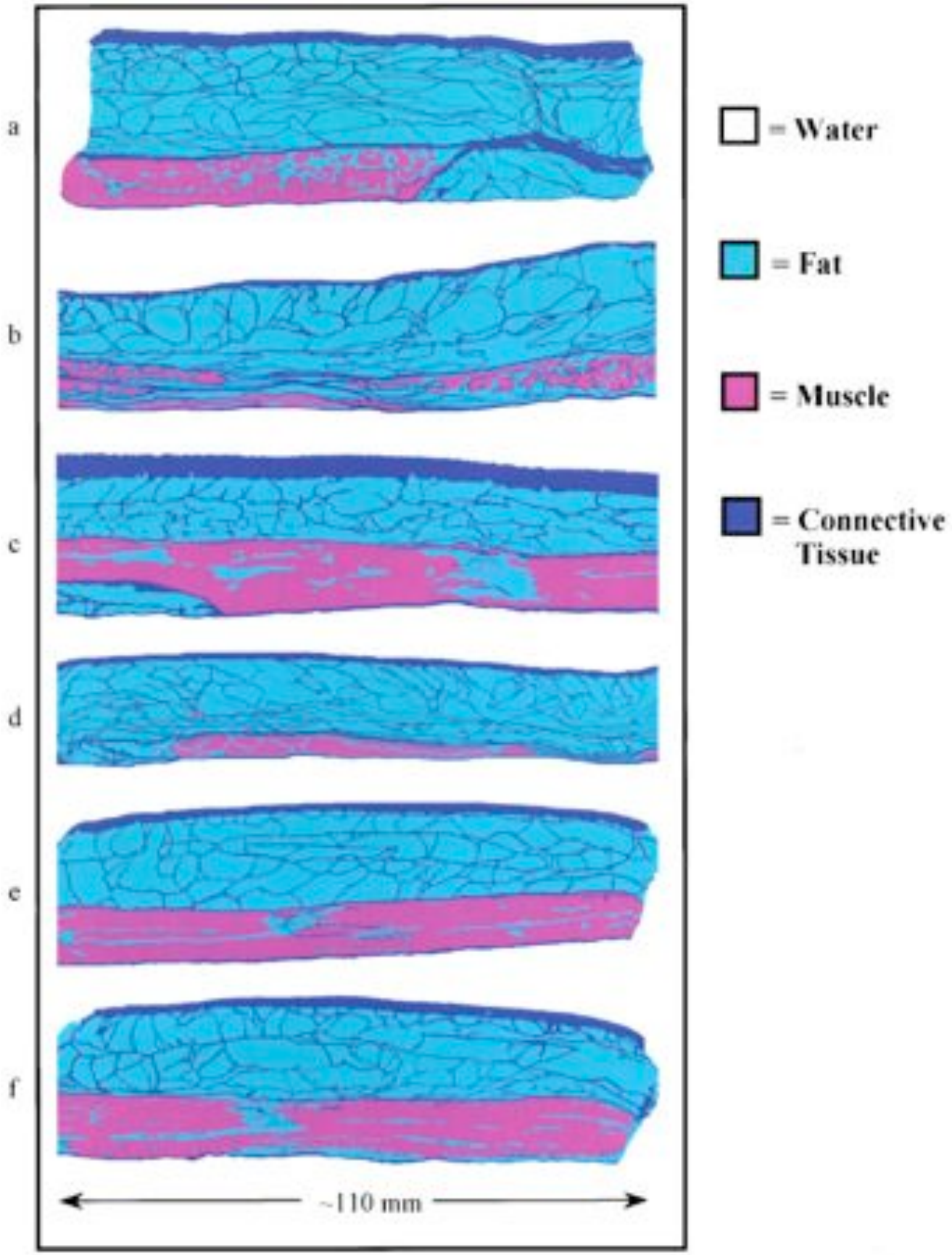

FIG. 3. Cross-sectional tissue maps. (a) 75hi. (b) 77ba. (c) 87de. (d) 102gh. (e) 120de. (f) 120fe. The number in each identifier refers to the donor of the specimen while the letters indicate the position of the cross section in the specimen.

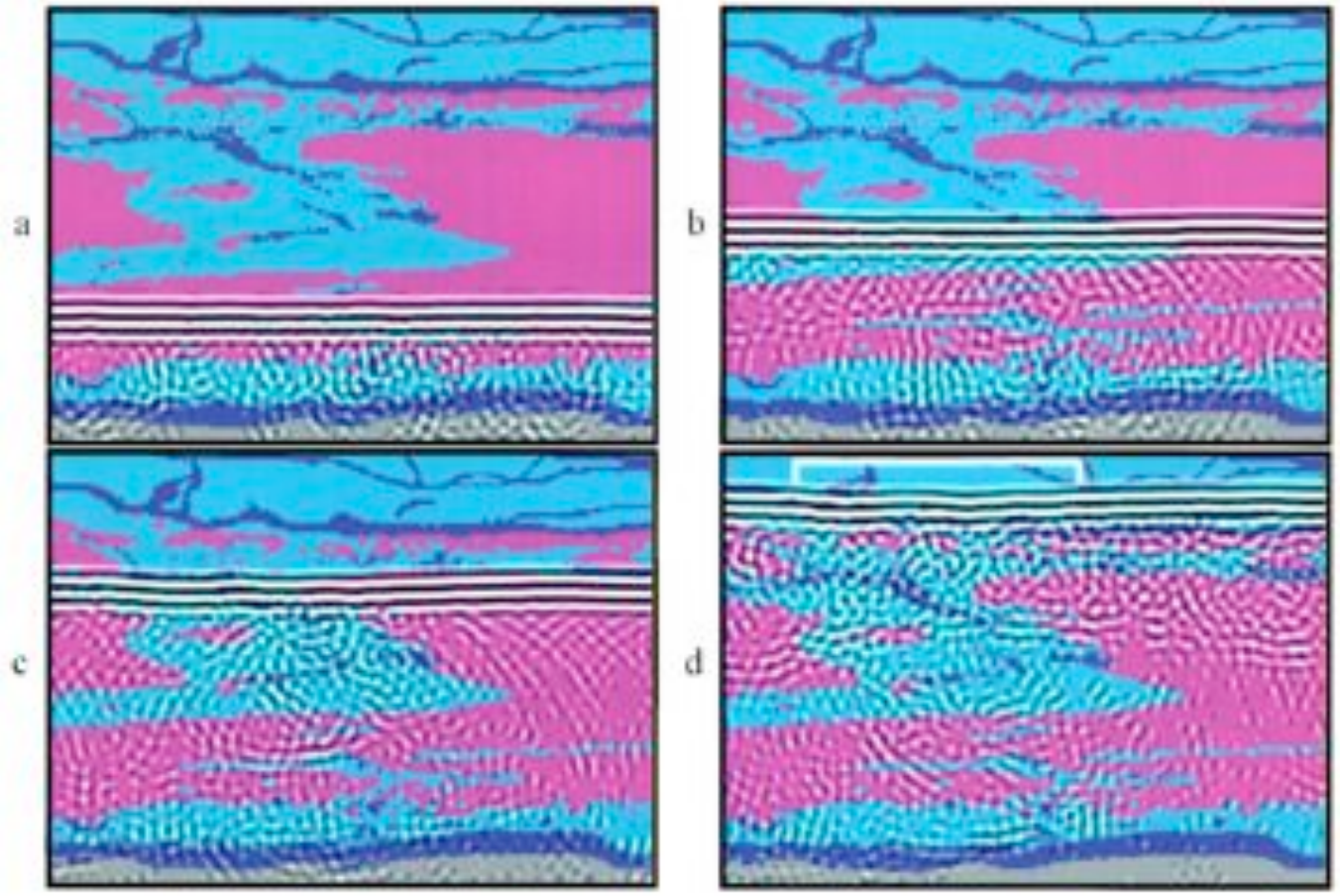

FIG. 4. Propagation through an aponeurosis in cross section 120fe. Panels (a)–(d) show the progression of the main wavefront through the muscle layer including an aponeurosis comprised of fat and connective tissue, resulting in time-shift aberration across the wavefront. The area shown in each frame is 16.0 mm in height and 18.7 mm in width. The temporal interval between frames is 1.7 μs. Tissue is shown using the same color scheme as in Fig. 3 while gray background represents water. Wavefronts are shown on a bipolar logarithmic scale with a 30 dB dynamic range. White represents maximum positive pressure and black represents maximum negative pressure. A cumulative delay of about 0.2 μs, associated with propagation through the aponeurosis, is indicated by the square bracket in panel (d).

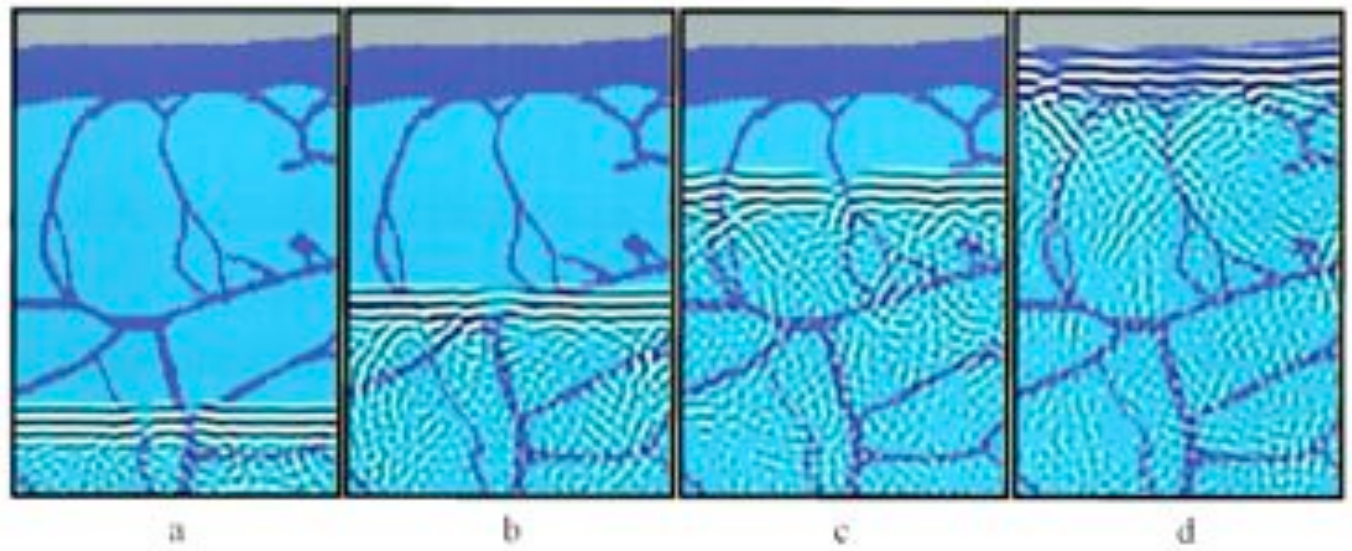

FIG. 5. Propagation through fat and septa in cross section 120fe. Panels (a)–(d) show the progression of the main wavefront through subcutaneous fat, showing the formation of amplitude dropouts by scattering from thin, near-vertically aligned septa. The area shown in each frame is 22.9 mm in height and 14.4 mm in width. The temporal interval between frames is 3.8 μs. The background medium and wavefronts are represented in the same manner as in Fig. 4.

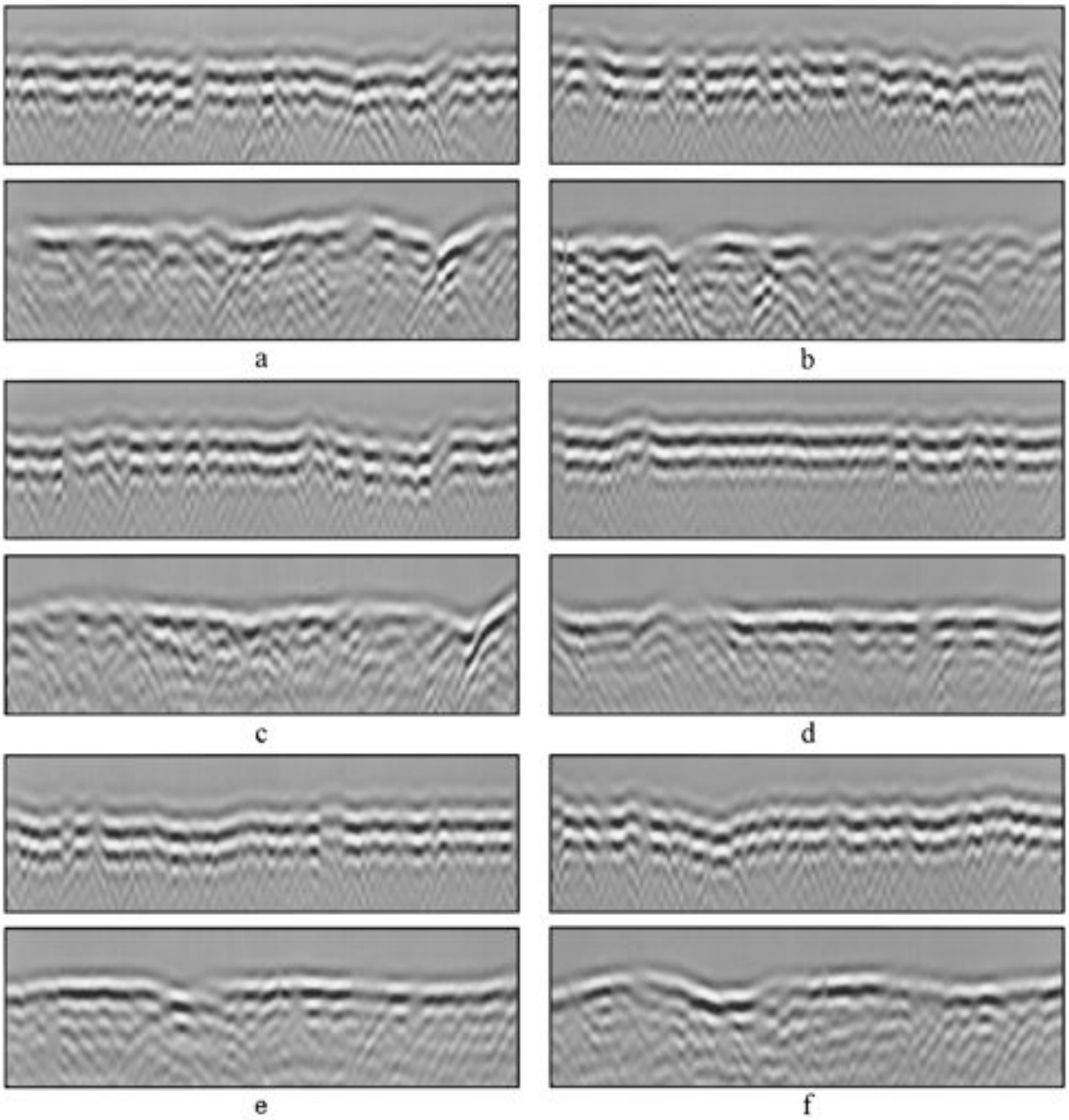

FIG. 6. Received wavefronts. In each pair, the top wavefront is the result of the FDTD propagation simulation for the given tissue map while the bottom is the corresponding experimentally measured wavefront. Wavefronts are shown on a linear gray scale with time as the vertical axis and element number as the horizontal axis. The temporal range shown is 2.0 μs for 128 elements. (a) Specimen 75hi. (b) Specimen 77ba. (c) Specimen 87de. (d) Specimen 102gh. (e) Specimen 120de. (f) Specimen 120fe.

example is associated with large-scale variations in sound speed rather than with other effects such as irregularity of the interfaces between tissue layers.

An example of amplitude dropout formation is shown in Fig. 5 using simulated internal wavefronts within cross section 120fe during propagation through the subcutaneous fat and septa. These results show the cumulative formation of amplitude fluctuations by scattering from septa aligned close to the main direction of propagation. As the wave propagates along a path that includes septa, energy is scattered outside the main direction of propagation. Scattered energy interferes constructively in a manner determined by the angle and contrast of the septa, so that secondary wavefronts are formed. Because the transmitted pulse is of short temporal duration (wide band), scattering from septa results in the removal of energy from the main wavefront, causing amplitude dropouts in the received waveforms. This effect is inherently different from effects of coherent interference that may occur for narrow band propagation through tissue.

Animated visualization of the saved pressure raster im-

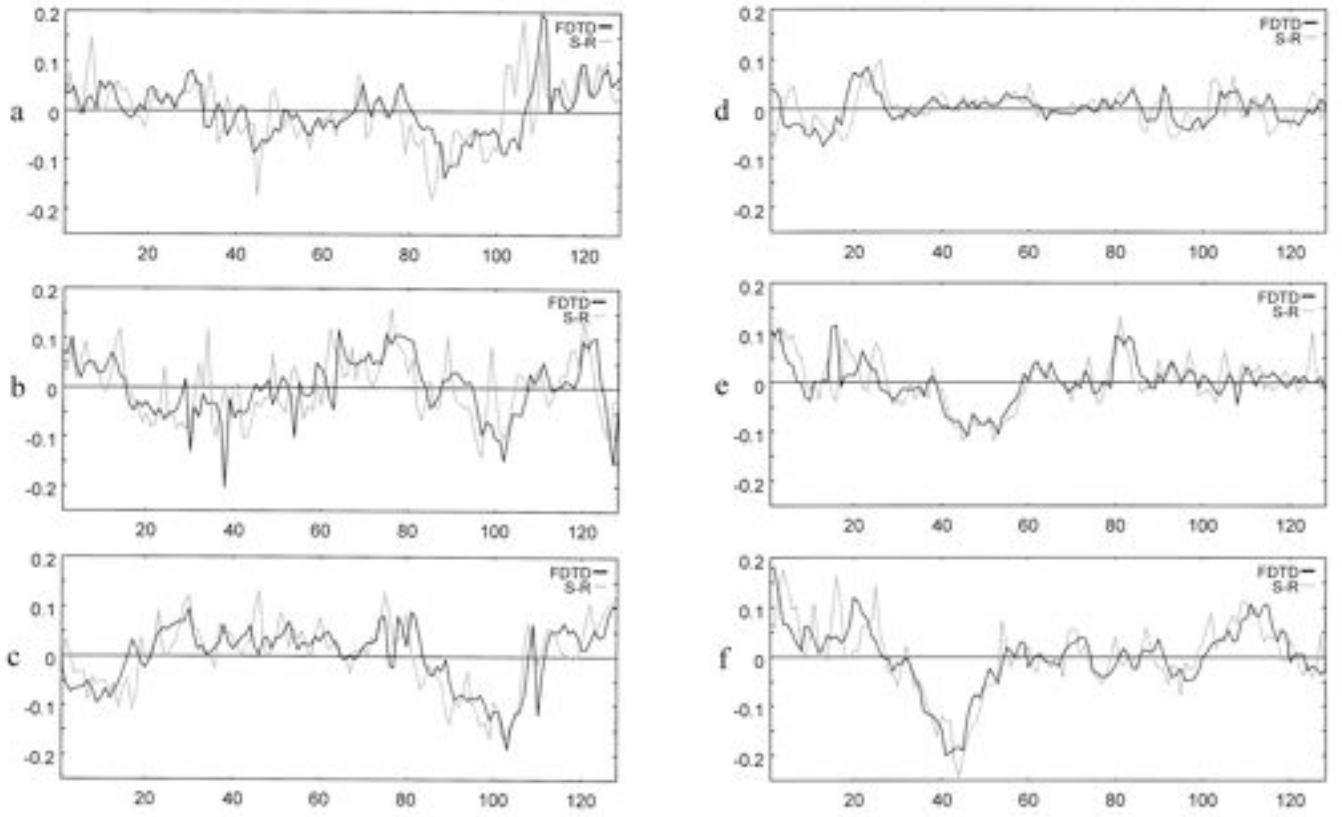

FIG. 7. Arrival time surfaces for FDTD and straight-ray (S-R) simulations. In each plot, the horizontal axis is the element number while the vertical axis is the arrival time fluctuation in microseconds, with positive values representing earlier arrivals. (a) Specimen 75hi. (b) Specimen 77ba. (c) Specimen 87de. (d) Specimen 102gh. (e) Specimen 120de. (f) Specimen 120fe.

ages was employed to gain insight into the development of wavefront distortion. This visualization clearly showed multiple scattering effects; for instance a secondary wavefront caused by scattering from one septum would be further scattered and distorted by other septa later in its propagation path. These effects lead to the complex, random wave field that appears behind the principal wavefront in Figs. 4 and 5.

Received wavefronts from the FDTD simulation are presented in Fig. 6 together with the corresponding experimentally measured wavefronts. The waveforms show qualitatively similar features, including the magnitude of large-scale time-shift and amplitude fluctuations as well as the presence of waveform distortion. However, the locations of these features do not match precisely between computed and experimentally measured wavefronts. Possible reasons for this discrepancy are given in Sec. IV.

Distortion statistics for the wavefronts determined by measurements and the FDTD and straight-ray simulations are given in Table II. The statistics of the FDTD results show qualitative agreement with the statistics of the experimental results. However, it may be noted that the arrival time and wave shape distortion in the simulated results are typically smaller than the measured distortion. Arrival time fluctuations from the FDTD results and from the straight-ray results are presented in Fig. 7. The corresponding energy level fluctuations are presented in Fig. 8. The statistics of each simulation are reported in Table II, while correlation coefficients for the arrival time surfaces and the energy level surfaces which result from the two types of simulation are reported in Table III. Arrival time surfaces calculated using the straight-ray method agree well with those predicted using the FDTD method, as seen by the correlation coefficients, which vary between 0.413 and 0.807. For the aperture size of 128 elements, a correlation coefficient with magnitude greater than 0.2875 is significant to a 99.9% confidence level.[42] This agreement provides evidence that time-shift aberration in the abdominal wall is, in many cases, principally associated with large-scale variations in sound speed. However, the energy level fluctuations calculated by the straight-ray approximation are much smaller in magnitude than those from the FDTD results and the experiments. The two sets of simulated energy level fluctuations are also poorly correlated. These results indicate that differences in the attenuation characteristics of the various tissue types at the center frequency of the transmitted pulse are inherently incapable of explaining the amplitude fluctuation that are observed both in experiments[2,3,5,6,22] and in our full-wave computations. Since the asymptotic straight-ray simulation neglected scattering and ray-bending effects that cause waveform distortion, waveform similarity factors reported in Table II are unity for the straight-ray simulation. More realistic waveform distortion was present in the FDTD simulations, but the amount of waveform distortion in the FDTD results, as quantified by the waveform similarity factor, was somewhat smaller than in the measurements.

The energy level fluctuations reported in Table II can be

TABLE II. Statistics of wavefront distortion from measurements (Exp.), finite-difference simulations (FDTD), and straight-ray simulations (S-R).

Specimen number	Specimen thickness (mm)	Data source	Arrival time fluctuations rms value (ns)	Arrival time fluctuations Correlation length (mm)	Energy level fluctuations rms value (dB)	Energy level fluctuations Correlation length (mm)	Waveform similarity factor
75hi	31–34	Exp.	92.7	4.10	3.85	2.99	0.873
		FDTD	53.0	2.72	3.29	1.25	0.957
		S-R	61.9	2.38	0.50	6.73	1.000
77ba	22–29	Exp.	102.7	3.61	3.98	2.38	0.841
		FDTD	59.9	3.75	4.44	1.17	0.951
		S-R	60.8	2.11	0.46	2.29	1.000
87de	26–30	Exp.	73.7	4.74	3.47	2.75	0.866
		FDTD	60.9	8.69	4.18	1.46	0.948
		S-R	67.8	7.66	0.46	5.23	1.000
102gh	17–21	Exp.	38.7	5.56	3.89	3.22	0.943
		FDTD	28.4	4.48	3.10	1.37	0.986
		S-R	32.3	2.24	0.25	2.57	1.000
120de	25–29	Exp.	59.5	5.76	3.07	2.35	0.958
		FDTD	43.6	2.26	3.28	1.38	0.980
		S-R	48.7	3.71	0.54	10.95	1.000
120fe	28–30	Exp.	73.8	8.66	3.66	3.71	0.914
		FDTD	67.1	4.47	3.41	1.30	0.983
		S-R	73.0	7.99	0.68	10.98	1.000

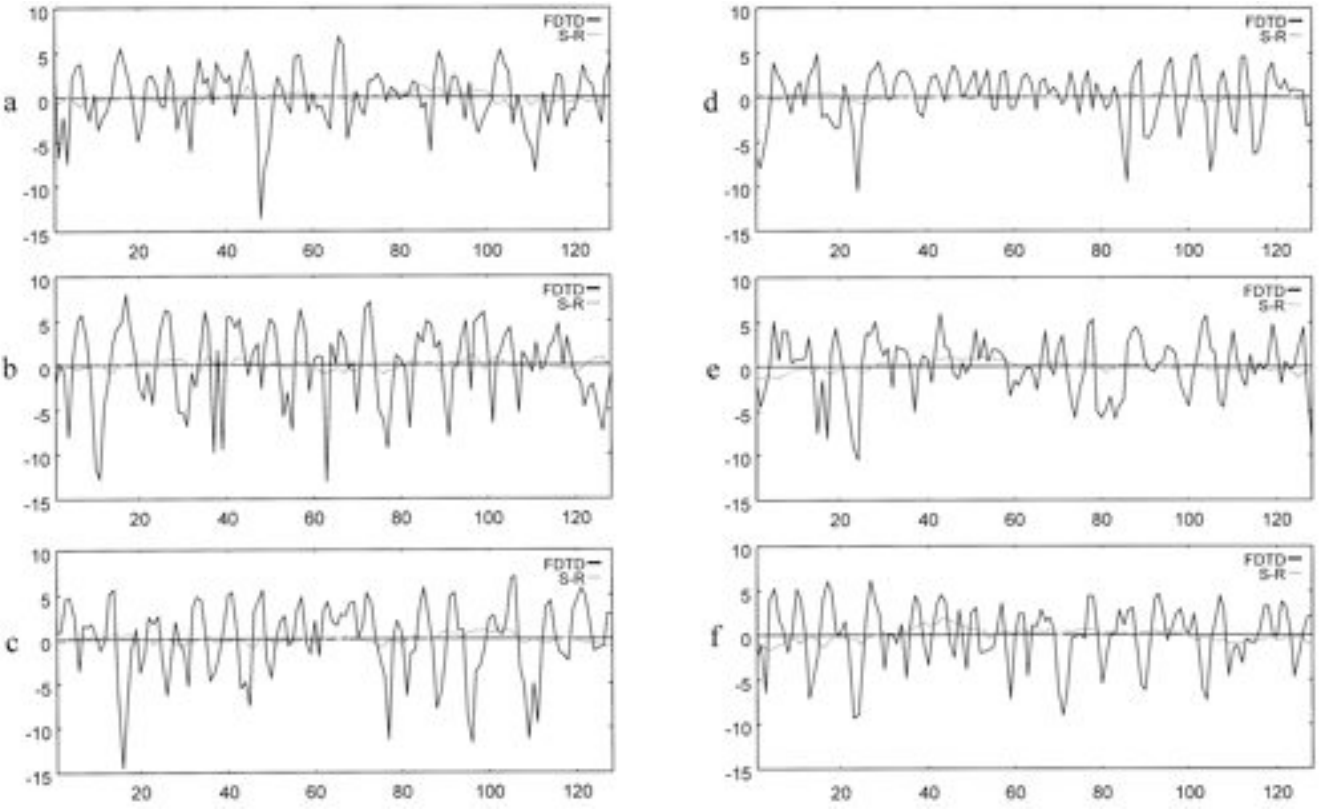

FIG. 8. Energy level surfaces for FDTD and straight-ray (S-R) simulations. In each plot, the horizontal axis is the element number while the vertical axis is the energy level fluctuation in dB, with positive values representing higher amplitudes. (a) Specimen 75hi. (b) Specimen 77ba. (c) Specimen 87de. (d) Specimen 102gh. (e) Specimen 120de. (f) Specimen 120fe.

TABLE III. Correlation coefficients between arrival time surfaces and energy level surfaces from FDTD and straight-ray simulations.

Specimen number	Arrival time correlation	Energy level correlation
75hi	0.508	−0.094
77ba	0.521	−0.051
87de	0.761	0.027
102gh	0.413	0.111
120de	0.693	−0.157
120fe	0.807	−0.065

used to classify ultrasonic scattering in the abdominal wall in terms of common nomenclature for propagation in random media. The rms values of the measured and simulated energy level fluctuations were within the range of 3.1–4.4 dB, which corresponds to a logarithmic amplitude variance of about 0.4–0.5. In a standard reference work on wave propagation in random media, wavefront fluctuations caused by scattering are defined to be weak only if the logarithmic amplitude variance is ''less than about 0.2–0.5.'' Otherwise, strong-fluctuation theory is required.[43] The wavefront distortion effects associated with ultrasonic propagation through the abdominal wall, therefore, should be considered within the range of strong fluctuations that cannot be described fully by weak scattering theory.

IV. DISCUSSION

The simulations and measurements reported here, like the measurements detailed in Refs. 1–6 and 22, model only part of the wavefront distortion that occurs in pulse-echo ultrasonic imaging systems. In the present simulations and experiments, the transmission configuration and broad wavefront model the return path of an initially coherent echo from a scattering site within the abdomen. A transmission configuration is generally used in distortion measurements because this simple arrangement allows the ultrasonic aberration produced by the tissue to be measured directly. However, in pulse-echo imaging, the echo coherence may also be reduced by degradation of the transmit focus. Thus, the distortion measured and calculated here can be regarded as a conservative estimate of the distortion that may be incurred in clinical imaging. In particular, echoes produced by diffuse inhomogeneities illuminated by a poorly-focused beam may be substantially more distorted than those described here.

The measurements and simulations presented here also differ from clinical ultrasonic imaging in that post mortem specimens are employed rather than living subjects. This allows experimental conditions to be controlled precisely and enables tissue morphology to be determined in detail by means of dissection and staining, but implies that the results may not correspond exactly to the clinical situation. It also requires the specimens to be subjected to some form of preservation to prevent degradation during the time between their acquisition, the making of measurements, and imaging for the simulations. The preservation methods used were chosen to minimize their impact on experimental results. For example, the specimens were frozen rather than fixed with formalin before the measurements because formalin fixation alters the elastic properties of tissue. Previous work[2] indicates that freezing affects distortion measurements minimally. The cellular disruption produced by freezing and thawing also should not affect the simulation results because it occurs on scales much smaller than the resolution of the images (0.5- to 20-μm cellular size versus 0.085-mm resolution). The cross sections are finally fixed in formalin because this is required for staining and because it allows them to be kept indefinitely for future reference.

The wavefronts computed using the finite-difference, time-domain method exhibit qualitative agreement with measured distortion for the same specimens. However, the simulated results do not show precise quantitative agreement with the measurements. Several reasons for these differences exist.

First, available computational resources limited the present simulations to a two-dimensional geometry, while real ultrasonic propagation through tissue occurs in three dimensions. Although the computation did not precisely simulate the physical situation of three-dimensional wavefront distortion, the two-dimensional computations are believed to yield a qualitatively accurate description of the development of wavefront distortion as an ultrasonic pulse propagates through abdominal wall. Two-dimensional computations may also be appropriate for characterization of the wavefront distortion that affects clinical imaging systems in which two-dimensional sections of tissue are imaged using a beam focused in the elevation direction. The lack of three-dimensionality is a likely explanation for some of the observed differences between the calculated and measured wavefronts.

Although care was taken to ensure that the sound speed, density, and attenuation parameters used were representative values for the tissues employed, no single group of parameters can characterize all tissue of a given type. As seen in Refs. 21, 37–39, and 41, measured ultrasonic tissue properties vary considerably among individual tissue specimens and different measurement techniques. The tissue model used in this study is also limited by the absence of tissue microstructure below a resolution of about 0.085 mm (corresponding to the 300 d.p.i. resolution of the scanned images employed) and point-to-point variations in sound speed and density within individual tissue types. Although these variations can be quantitatively estimated using acoustic microscopy,[21,39] implementation of this process with high resolution is not practically feasible for large cross sections like those used in the present study. Further limitations arose from the neglect of anisotropy in tissue properties. An extended tissue model could incorporate these effects into similar computations, given that the orientation of each tissue type were known. The approximate nature of the tissue model presented here is an additional cause for the lack of precise quantitative agreement between the simulated and measured wavefronts.

A high degree of uniformity in the received waveforms is necessary for accurate estimation of pulse arrival times when a correlation-based estimation method is used.[44] Table II and Fig. 6 indicate that the measured waveforms are more distorted than those produced by the finite-difference, time-

domain simulation. This may be related to the difference in dimensionality of the distortion encountered in the two cases. Whatever the cause, the result is that the arrival times estimated for the FDTD data are likely to be more accurate than those determined for the corresponding measurements. This could also account for the lower arrival time fluctuation rms values obtained for the FDTD simulation results.

Several other assumptions of the FDTD model were considered not to affect the results significantly. First, no damping was formally incorporated into the finite-difference time-domain model, although the computational method used is slightly dissipative (see Ref. 25 for a discussion of numerical dissipation in finite-difference algorithms). However, the straight-ray attenuation calculations confirm that amplitude fluctuations caused by varying tissue attenuation are much smaller than those caused by scattering effects, so that any artifacts caused by the absence of explicit absorption or the presence of numerical dissipation did not significantly impact the results. The shear elasticity of tissue was neglected in our calculations because tissue has been found to be well approximated by a fluid model at frequencies used in diagnostic ultrasound.[45,46] Therefore, the absence of attenuation and shear elasticity from our FDTD simulations, as well as the small numerical dissipation associated with the finite-difference algorithm, do not affect the validity of our distortion results.

Despite the limitations of the model employed, the presence of realistic time-shift aberrations, amplitude drop outs, and waveform fluctuations indicate that the FDTD method and tissue model employed in this study are sufficient to explain the principal characteristics of wavefront distortion produced by the abdominal wall. The model is, therefore, a useful tool for investigation of the physical causes of wavefront distortion. In particular, the results have shown the formation of large-scale time-shift aberrations with propagation through slowly-varying tissue structures as well as strong amplitude and waveform distortion caused by scattering from inhomogeneities within subcutaneous fat. The computational model presented here is also potentially useful as a tool for the simulation of realistic scattering data for tests of focusing and imaging algorithms.

Since many previous studies of ultrasound-tissue interaction have been based on weak scattering models such as the Born and Rytov approximations,[20,21,47] it is notable that the present calculations show strong scattering and multiple scattering effects not predicted by such simple methods. For example, the large amplitude drop outs seen in the transmitted wavefronts are inconsistent with the Born *ansatz* that the incident wavefront is unperturbed by the scattering medium. Furthermore, examination of the internally scattered fields indicates that a single portion of an ultrasonic wavefront may incur scattering by several inhomogeneities over the large thickness of the abdominal wall, so that single-scattering approximations are seen to provide incomplete representations of the wave effects occurring in real tissue.

Finally, the results reported here clearly show that simple phase-screen and amplitude-screen models do not fully characterize ultrasonic propagation through the abdominal wall. The straight-ray simulation performed in this study is equivalent to a simulation using both a phase and an amplitude screen at the receiving aperture, with time-shift and amplitude-shift values determined by integration of the local tissue sound speed and attenuation along straight propagation paths. Figures 7 and 8 and Tables II and III show that this simple model successfully predicts the magnitudes and large-scale trends of time-shift fluctuations, but is unable to predict energy-level fluctuations and waveform distortions that occur both in experimental measurements and in the full-wave computations reported here. More sophisticated models that include a phase screen some distance from the aperture do predict amplitude and waveform distortion[48–50] and are thus more successful in characterizing propagation through the abdominal wall, as seen from the improved performance of correction algorithms incorporating these models.[6,13] However, no single phase screen, whether alone or in combination with an amplitude screen, can cause cumulative propagation effects and strong scattering effects like those obtained using the present full-wave model and illustrated by Figs. 4 and 5. These effects could be represented, at least in part, by more sophisticated models that include multiple phase screens or numerical ray tracing, but since such models are based on further approximations to the wave propagation equations considered here, they are less complete than the present full-wave approach.

The observation that single phase- and amplitude-screen models are incomplete implies that methods of wavefront distortion correction employing these models should not be expected to restore an ultrasonic focus aberrated by the abdominal wall to its diffraction-limited form. Such algorithms, which were originally developed to correct weak fluctuations such as may occur in radio astronomy, are not fully applicable to correction of strong scattering effects like those shown here to occur within the abdominal wall. Still, the performance of aberration correction algorithms to date suggests that improved models of propagation through tissue, such as the model of a phase screen away from the receiving aperture, have resulted in improved aberration correction. Aberration correction methods that incorporate some of the wave effects shown here could result in further improvements in ultrasonic focusing through the abdominal wall.

V. CONCLUSIONS

A new model for ultrasonic propagation through abdominal wall has been presented. The model is based on realistic cross-sectional tissue maps and on a full-wave solution of the acoustic propagation equations for an inhomogeneous fluid medium.

The model produces wavefront distortion that is statistically similar to experimentally measured wavefront distortion for the same tissue specimens. Some major features of the experimentally measured distortion are reproduced; however, accurate simulation of the precise structure of received wavefronts may require three-dimensional computation as well as more complete tissue models.

Visualization of ultrasonic wavefronts inside the abdominal wall shows the development of time-shift fluctuations as the wavefront propagates through large-scale tissue variations. Examination of the internal pressure fields also

shows that large amplitude and waveform fluctuations can be caused by scattering from high-contrast inhomogeneities such as vertically-aligned septa within the subcutaneous fat layer.

Comparison of the finite-difference, time-domain results with results of a straight-ray approximation suggests that a significant portion of the time-shift aberration caused by the abdominal wall can be explained using simple phase-screen models. However, these models, even those that incorporate tissue attenuation variations, are unable to completely predict amplitude and waveform distortion caused by the abdominal wall. Since these latter distortion effects are associated with strong scattering, complete correction of amplitude and waveform distortion is a challenge that may not be fully attainable using currently available methods of aberration correction that model the aberrating layer as a phase screen alone or in combination with an amplitude screen. Progress toward the goal of diffraction-limited focusing through the abdominal wall may be achieved by incorporation of wave effects such as strong scattering into aberration correction algorithms.

ACKNOWLEDGMENTS

The authors thank Dr. Leon Metlay, Mark Burkard, Cari Kelly, Brian Williams, Georgia Gianakakos, and Kaushik Mittra for assistance in creating accurate tissue maps of the abdominal wall cross sections. Dong-Lai Liu is thanked for providing the original two-dimensional version of the distortion estimation software using the reference waveform method. Funding for this investigation was provided by the University of Rochester Diagnostic Ultrasound Research Laboratory Industrial Associates, NIH Grants Nos. DK 45533 and HL 50855, US Army Grant No. DAMD-17-94-J-4384, and the F. V. Hunt Fellowship of the Acoustical Society of America. Computations were performed at the Cornell National Supercomputing Facility, which is supported in part by the National Science Foundation, New York State, and the IBM Corporation, and at the Center for Academic Computing of the Pennsylvania State University.

[1] Y. Sumino and R. C. Waag, ''Measurements of ultrasonic pulse arrival time differences produced by abdominal wall specimens,'' J. Acoust. Soc. Am. **90**, 2924–2930 (1991).
[2] L. M. Hinkelman, D.-L. Liu, L. A. Metlay, and R. C. Waag, ''Measurements of ultrasonic pulse arrival time and energy level variations produced by propagation through abdominal wall,'' J. Acoust. Soc. Am. **95**, 530–541 (1994).
[3] L. M. Hinkelman, T. L. Szabo, and R. C. Waag, ''Measurements of ultrasonic pulse distortion produced by the human chest wall,'' J. Acoust. Soc. Am. **101**, 2365–2373 (1997).
[4] P. D. Freiburger, D. C. Sullivan, B. H. LeBlanc, S. W. Smith, and G. E. Trahey, ''Two dimensional ultrasonic beam distortion in the breast: In vivo measurements and effects,'' Ultrason. Imaging **14**, 398–414 (1992).
[5] Q. Zhu and B. D. Steinberg, ''Large-transducer measurements of wavefront distortion in the female breast,'' Ultrason. Imaging **14**, 276–299 (1992).
[6] L. M. Hinkelman, D.-L. Liu, R. C. Waag, Q. Zhu, and B. D. Steinberg, ''Measurement and correction of ultrasonic pulse distortion produced by the human breast,'' J. Acoust. Soc. Am. **97**, 1958–1969 (1995).
[7] G. Kossoff, D. A. Carpenter, D. E. Robinson, D. Ostry, and P. L. Ho, ''A sonographic technique to reduce beam distortion by curved interfaces,'' Ultrasound Med. Biol. **15**, 375–382 (1989).
[8] S. W. Smith, G. E. Trahey, and O. T. von Ramm, ''Phased array ultrasound imaging through planar tissue layers,'' Ultrasound Med. Biol. **12**, 229–243 (1986).
[9] M. O'Donnell and S. W. Flax, ''Phase-aberration correction using signals from point reflectors and diffuse scatterers: Measurements,'' IEEE Trans. Ultrason. Ferroelectr. Freq. Control **35**, 768–774 (1988).
[10] L. Nock, G. E. Trahey, and S. W. Smith, ''Phase aberration correction in medical ultrasound using speckle brightness as a quality factor,'' J. Acoust. Soc. Am. **85**, 1819–1833 (1989).
[11] D. Rachlin, ''Direct estimation of aberrating delays in pulse-echo imaging systems,'' J. Acoust. Soc. Am. **88**, 191–198 (1990).
[12] M. Hirama, O. Ikeda, and T. Sato, ''Adaptive ultrasonic array imaging through an inhomogeneous layer,'' J. Acoust. Soc. Am. **71**, 100–109 (1982).
[13] D.-L. Liu and R. C. Waag, ''Correction of ultrasonic wavefront distortion using backpropagation and a reference waveform method for time-shift compensation,'' J. Acoust. Soc. Am. **96**, 649–660 (1994).
[14] C. Dorme and M. Fink, ''Ultrasonic beam steering through inhomogeneous layers with a time reversal mirror,'' IEEE Trans. Ultrason. Ferroelectr. Freq. Control **43**, 167–175 (1996).
[15] S. Krishnan, P.-C. Li, and M. O'Donnell, ''Adaptive compensation for phase and magnitude aberrations,'' IEEE Trans. Ultrason. Ferroelectr. Freq. Control **43**, 44–55 (1996).
[16] D. E. Robinson, L. S. Wilson, and G. Kossoff, ''Shadowing and enhancement in ultrasonic echograms by reflection and refraction,'' J. Clin. Ultrasound **9**, 181–188 (1981).
[17] E. E. Sauerbrei, ''The split image artifact in pelvic ultrasonography: the anatomy and physics,'' J. Ultrasound Med. **4**, 29–34 (1985).
[18] C. W. Manry, Jr., and S. L. Broschat, ''FDTD simulations for ultrasound propagation in a 2-D breast model,'' Ultrason. Imaging **18**, 25–34 (1996)
[19] A. P. Berkhoff, P. M. van den Berg, and J. M. Thijssen, ''Simulation of wave propagation through aberrating layers of biological media,'' 1994 IEEE Ultrason. Symp. Proc. **3**, 1797–1800 (1994).
[20] R. C. Waag, J. O. Nilsson, and J. P. Astheimer, ''Characterization of volume scattering power spectra in isotropic media from power spectra of scattering by planes,'' J. Acoust. Soc. Am. **74**, 1555–1571 (1983).
[21] F. L. Lizzi, M. C. Rorke, D. L. King, E. J. Feleppa, A. Kalisz, J. B. Sokil-Melgar, and J. Nowakowski, ''Simulation studies of ultrasonic backscattering and B-mode images of liver using acoustic microscopy data,'' IEEE Trans. Ultrason. Ferroelectr. Freq. Control **39**, 212–226 (1992).
[22] B. S. Robinson, A. Shmulewitz, and T. M. Burke, ''Waveform aberrations in an animal model,'' 1994 IEEE Ultrason. Symp. Proc. **3**, 1619–1624 (1994).
[23] A. D. Pierce, *Acoustics: An Introduction to its Physical Principles and Applications* (Acoustical Society of America, Woodbury, New York, 1989), 2nd ed., pp. 14–17.
[24] R. W. MacCormack, *Lecture Notes in Physics* (Springer-Verlag, Berlin, 1971), Vol. 8, p. 151.
[25] D. Gottlieb and A. Turkel, ''Dissipative two-four methods for time-dependent problems,'' Math. Comput. **30**, 703–723 (1976).
[26] V. W. Sparrow and R. Raspet, ''A numerical method for general finite amplitude wave propagation and its application to spark pulses,'' J. Acoust. Soc. Am. **90**, 2683–2691 (1991).
[27] P. M. Morse and K. U. Ingard, *Theoretical Acoustics* (McGraw-Hill, New York, 1968), p. 464.
[28] R. L. Burden, J. D. Faires, and A. C. Reynolds, *Numerical Analysis* (Prindle, Weber, and Schmidt, Boston, 1978), p. 380.
[29] The hemispheric source was constructed by Hans Persson of the Department of Electrical Measurements, Lund University, Lund, Sweden.
[30] The linear array employed was a Toshiba model PLE-308M.
[31] L. M. Hinkelman, L. A. Metlay, C. J. Churukian, and R. C. Waag, ''Modified Gomori trichrome stain for macroscopic tissue slices,'' J. Histotech. **19**(4), 321–323 (1996).
[32] The images were processed using Adobe Photoshop, version 3.0.
[33] E. Turkel, ''On the practical use of high-order methods for hyperbolic systems,'' J. Comp. Phys. **35**, 319–340 (1980).
[34] N. Bilaniuk and G. S. K. Wong, ''Speed of sound in pure water as a function of temperature,'' J. Acoust. Soc. Am. **93**, 1609–1612 (1993).
[35] *Handbook of Chemistry and Physics*, edited by R. C. Weast (CRC, Boca Raton, 1985), p. F-10.
[36] K. H. Herzfeld and T. A. Litovitz, *Absorption and Dispersion of Ultrasonic Waves* (Academic, New York, 1959), pp. 353–361.
[37] S. A. Goss, R. L. Johnston, and F. Dunn, ''Comprehensive compilation of

empirical ultrasonic properties of mammalian tissues,'' J. Acoust. Soc. Am. **64**, 423–457 (1978).
[38] S. A. Goss, R. L. Johnston and F. Dunn , ''Compilation of empirical ultrasonic properties of mammalism tissues II,'' J. Acoust. Soc. Am. **68**, 93–108 (1980).
[39] J. E. Olerud, W. O'Brien, M. A. Riederer-Henderson, D. Steiger, F. K. Forster, C. Daly, D. J. Ketterer, and G. F. Odland, ''Ultrasonic assessment of skin and wounds with the scanning laser acoustic microscope,'' J. Invest. Derm. **8**(5), 615–623 (1987).
[40] R. E. Neuman and M. A. Logan, ''The determination of collagen and elastin in tissues,'' J. Biol. Chem. **186**, 549–556 (1950).
[41] H. Q. Woodard and D. R. White, ''The composition of body tissues,'' Br. J. Radiol. **59**(708), 1209–1219 (1986).
[42] P. R. Bevington, *Data Reduction and Error Analysis for the Physical Sciences* (McGraw-Hill, New York, 1969), pp. 310–311.
[43] A. Ishimaru, *Wave Propagation and Scattering in Random Media* (Academic, New York, 1978), Vol. 2, Chap. 20.
[44] G. C. Ng, S. S. Worrell, P. D. Freiburger, and G. E. Trahey, ''A comparative evaluation of several algorithms for phase aberration correction,'' IEEE Trans. Ultrason. Ferroelectr. Freq. Control **41**, 631–643 (1994).
[45] L. A. Frizzell, E. L. Carstensen, and J. F. Dyro, ''Shear properties of mammalism tissues at low MHz frequencies,'' J. Acoust. Soc. Am. **60**, 1409–1411 (1976).
[46] E. L. Madsen, H. J. Sathoff, and J. A. Zagzebski, ''Ultrasonic shear wave properties of soft tissues and tissuelike materials,'' J. Acoust. Soc. Am. **74**, 1346–1355 (1983).
[47] R. C. Waag, D. Dalecki, and W. A. Smith, ''Estimates of wave front distortion from measurements of scattering by model random media and calf liver,'' J. Acoust. Soc. Am. **85**, 406–415 (1989).
[48] A. Hewish, ''The diffraction of radio waves in passing through a phase-changing ionosphere,'' Proc. R. Soc. London, Ser. A **209**, 81–96 (1951).
[49] R. P. Mercier, ''Diffraction by a screen causing large random phase fluctuations,'' Proc. Camb. Philos. Soc. A **58**, 382–400 (1962).
[50] A. D. Pierce, ''Spikes on sonic boom pressure waveforms,'' J. Acoust. Soc. Am. **46**, 1366–1380 (1968).